

## Urban land-use land-cover extraction for catchment modelling using deep learning techniques

Siming Gong <sup>\*</sup>, James Ball  and Nicholas Surawski 

Faculty of Engineering and Information Technology, University of Technology Sydney, 15 Broadway, Ultimo NSW 2007, Australia

\*Corresponding author. E-mail: [siming.gong@student.uts.edu.au](mailto:siming.gong@student.uts.edu.au)

 SG, 0000-0003-4244-1181; JB, 0000-0001-8342-1916; NS, 0000-0003-2584-1044

### ABSTRACT

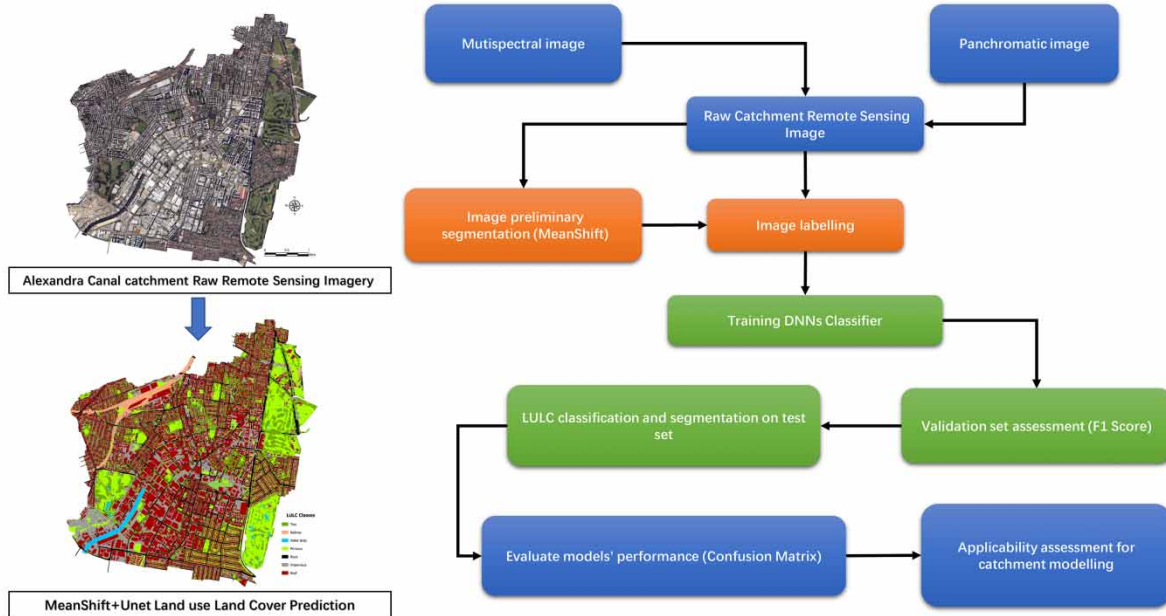
Throughout the world, the likelihood of floods and managing the associated risk are a concern to many catchment managers and the population residing in those catchments. Catchment modelling is a popular approach to predicting the design flood quantiles of a catchment with complex spatial characteristics and limited monitoring data to obtain the necessary information for preparing the flood risk management plan. As an important indicator of urbanisation, land use land cover (LULC) plays a critical role in catchment parameterisation and modelling the rainfall-runoff process. Digitising LULC from remote sensing imagery of urban catchment is becoming increasingly difficult and time-consuming as the variability and diversity of land uses occur during urban development. In recent years, deep learning neural networks (DNNs) have achieved remarkable image classification and segmentation outcomes with the powerful capacity to process complex workflow and features, learn sophisticated relationships and produce superior results. This paper describes end-to-end data assimilation and processing path using U-net and DeepLabV3+, also proposes a novel approach integrated with the clustering algorithm MeanShift. These methods were developed to generate pixel-based LULC semantic segmentation from high-resolution satellite imagery of the Alexandria Canal catchment, Sydney, Australia, and assess the applicability of their outputs as inputs to different catchment modelling systems. A significant innovation is using the MeanShift clustering algorithm to reduce the spatial noise in the raw image and propagate it to the deep learning network to improve prediction. All three methods achieved excellent classification performance, where the MeanShift+U-net has the highest accuracy and consistency on the test imagery. The final suitability assessment illustrates that all three methods are more suitable for the parameterisation of semi-distributed modelling systems rather than the fully distributed modelling systems, where the MeanShift+U-net should be adopted for image-based impervious area extraction of urban catchment due to its superior prediction accuracy of 98.47%.

**Key words:** catchment modelling, deep learning, land use land cover (LULC), remote sensing

### HIGHLIGHTS

- Urban land-use land-cover semantic segmentation and classification.
- Deep learning techniques for parameter estimation.
- Computer vision analysis of remote sensing data.
- Intergration of deep learning neural networks and clustering algorithm.
- Suitability of AI techniques for estimating spatially distributed parameters.

## GRAPHICAL ABSTRACT



## Urban Land Use Land Cover Extraction for Catchment Modelling Using Deep Learning Techniques

### INTRODUCTION

Floods are one of the most destructive and frequent natural disasters, causing many personnel casualties and property losses every year (Dawson *et al.* 2008; Jha *et al.* 2012; Zaman *et al.* 2012; Willner *et al.* 2018). The process of urbanisation has increased the flood risk to human society with the rapid growth of impervious areas such as buildings, roads and parking areas, which break the infiltration of stormwater to the deep soil and permanently change the natural rainfall–runoff process of the catchment (Arnold & Gibbons 1996; Jha *et al.* 2012; Ball *et al.* 2019). Unlike the nature catchment, the impervious surface degrades nature flood resilience by directly transferring rainfall to runoff, which increases the flood volume and leads to the earlier arrival of the flood peak (Holman-Dodds *et al.* 2003; Li *et al.* 2017). The weakening of catchment nature flood resilience results in the vulnerability of communities to flood when exposed to the storm burst beyond the capacity of the urban stormwater drainage system. In addition, other factors such as climate change, irresponsible and inappropriate city planning and stormwater management strategies are growing trends that aggravate the devastation of floods in urban areas.

To understand the rainfall and runoff processes that interconnect the catchment hydrological components of a catchment and to further study the occurrence and consequence of flood events, catchment models were introduced to predict the catchment response to rainfall; limitations of measurement techniques and extremely complicated inner mechanism of catchment hydrology also encouraged the development of catchment models (Beven 2012; Peel & McMahon 2020). In the computer era, distributed catchment modelling systems have experienced significant progress with the development of remote sensing technology, geographic information system (GIS) and increased computation power (Salvadore *et al.* 2015); all of these developments allow the modeller to reproduce the catchment rainfall–runoff process at a scale suitable for the available data. These sophisticated catchment models require a mass of catchment data and the associated data digitalisation, assimilation, interpretation, parameterisation and calibration to maintain the robustness of the model predictions. Meanwhile, data quality and quantity are more important than ever before; the adequacy and reliability of a dataset play a critical role in the model performance (Gan *et al.* 1997). However, identification and digitisation of the spatial characteristics of urban catchments such as land use land cover (LULC) have become a significant problem that plagues many aspects (e.g. catchment modelling and urban planning) with the expansion of urban areas and the changing of land use (Liu *et al.* 2015; Hu *et al.* 2016). The

importance of land-use information for catchment modelling systems is reflected in determining the impervious ratio, infiltration rate and the associated surface roughness coefficient (e.g. Manning's  $n$  value) (Ball *et al.* 2019). Therefore, quickly providing accurate and reliable datasets to parameterise the catchment spatial characteristics for modelling purposes has become a topic that needs to be solved in the modelling community (Abulohom *et al.* 2001; Ball *et al.* 2019; Peel & McMahon 2020).

Breakthroughs in remote sensing techniques allow modellers to obtain numerous catchment spatial data with a visualisation form (Wulder *et al.* 2012). A typical representative of visualised catchment spatial data is the remote sensing imagery, which has become the indispensable dataset of catchment modelling systems (Klein & Barnett 2003; Mackay *et al.* 2003; Beven 2012). The interpretation of spatial information from the remote sensing imagery is required to estimate the parameters for catchment modelling purposes (Foody 2004). This interpretation includes identification, delineation and digitalisation of LULC (e.g. road, building, impervious/pervious area, vegetation and waterbody) (Boegh *et al.* 2004), which are time-consuming and require solid geographic knowledge (Niemi *et al.* 2019). In addition, the accuracy and reliability of the manual interpretation solely rely on the interpreter's ability and cannot be reproduced by other modelling groups or systems. This reduces the model's consistency when the catchment is experiencing LULC changes.

In recent years, the development of deep learning techniques has greatly facilitated the development of computer vision (CV) applications; the CV is a subbranch of machine learning with interdisciplinary knowledge involving how computers acquire information, process data and gain advanced understanding from digital images or videos (Voulodimos *et al.* 2018; Szeliski 2010). Examples of CV applications can be found in autonomous driving (Grigorescu *et al.* 2020), face recognition (Parkhi *et al.* 2015), image classification and segmentation (Ronneberger *et al.* 2015; He *et al.* 2017).

Meanwhile, deep learning has also achieved excellent performances in remote sensing applications. For example, Rezaee *et al.* (2018) proposed a deep learning neural network (DNN) to classify wetlands from remote sensing imagery. Zhao *et al.* (2017) introduced an object-based convolutional neural network to discriminate building types and footprints in a catchment of Beijing and achieved over 90% accuracy. Huang *et al.* (2018) modified the classic DNN architecture to adapt the multi-spectral data of high-resolution remote sensing imagery and achieved 91.25% precision in the land-use classification for the study area of Shenzhen and Hong Kong. Yang & Li (2015) used the linear spectral unmixing method to conquer the effect of vegetation for extracting road from an urban remote sensing image. In summary, these works focus on extracting individual spatial features or classifying images with low LULC heterogeneity (e.g. rural catchments and urban catchments with low landscape coverage). There is no universal methodology for modelling urban catchments, particularly in high heterogeneous LULC areas such as various landscape coverage and diverse building types (Salvadore *et al.* 2015); whether deep learning can achieve classification and segmentation of LULC for parameterising and modelling urban catchment, extensive research has not yet been undertaken.

Inspired by related works, this research develops a novel approach utilising a deep learning-based CV tool. This approach aims to produce the LULC classification and segmentation of urban catchment remote sensing imagery with heterogeneous spatial features and present a reproducible workflow for any other Australian urban catchment under the same remote sensing database. The feasibility and practicability of this approach for catchment modelling systems are discussed also. The remainder of this paper is organised as follows. Following the introduction, the study catchment is described, the proposed approach. The section 'Result and discussion' demonstrates the outputs and discusses their suitability for catchment modelling. Finally, the section 'Conclusion' presents the conclusions derived from the research.

## STUDY CATCHMENT

The Alexandra Canal catchment was selected as the test area for this study. This catchment is located south of the great Sydney CBD area, Australia. The catchment area is 11.50 square km and consists of four highly urbanised regions: Sheas Creek, Rosebery, Munni Street-Erskineville and Alexandra Canal, with multiple land uses inclusive of residential (approximately 40%), industrial (approximately 25%), road (approximately 10%), parkland (approximately 22%) and water body (approximately 3%). The catchment land covers are varied and include single dwelling, terrace, dense apartment, industrial plants with large impervious areas and sizeable pervious areas of parkland and golf courses. The drainage system of the Alexandra Canal catchment consists of subsurface pipes, pits, subsurface channels, open channels, culverts and flood mitigation structures. The location of the catchment with respect to continental Australia and within the greater Sydney region is shown in Figure 1 (Esri 2021).



**Figure 1** | Location of the Alexandria Canal catchment.

A significant feature of the catchment is the high heterogeneous LULC, such as the various roof colours and shapes, perennial vegetations, water bodies, railways, walking trails, roads, large pavement areas and buildings' shadows. A few ground features are difficult to identify on the imagery due to the obscuration of tree canopies. Additionally, in some regions of the catchment, the land zoning has changed from industrial land to commercial or residential land, leading to discontinuities in land cover between the expected and actual. The identification of these spatial features is essential for the catchment model. For example, a critical inferred control parameter 'Impervious percentage' in the stormwater management model (SWMM) is highly related to the measured geometry of catchment LULC and associated roughness coefficient, which requires the modeller to identify and delineate all impermeable ground features (e.g. roof and road) (Choi & Ball 2002). In summary, the LULC identification and classification of the catchment is a complex and very challenging task from the perspective of both CV and catchment modelling.

## METHODOLOGY

### Outline of methodology

The proposed LULC classification and segmentation methods of the catchment imagery consist of three algorithms, which are the clustering algorithm MeanShift (Cheng 1995), and the pixel classifiers U-net (Ronneberger *et al.* 2015) and DeepLabV3+ (Chen *et al.* 2018).

In the beginning, the catchment raw imagery was pre-processed to adapt to the deep learning environment. The MeanShift clustering algorithm was introduced to simplify the spectral information of the catchment imagery by producing a preliminary segmentation result. The segmented image was then used as the input of the pixel classifier U-net. Pure U-net and DeepLabV3+ classifiers were also implemented to classify and segment the LULC information using the catchment raw image as input for the control experiment. Then, the *F1* score was adopted to evaluate the models' prediction accuracy on the validation set, and the associated images to demonstrate the bias between the ground truth and classification outputs.

Finally, the performance of trained models on the test set was quantified using the confusion matrix to assess LULC accuracy associated with different catchment modelling systems. In machine learning, both the *F1* score and confusion matrix are effective measures to analyse the accuracy of the model's prediction, where the *F1* score is the harmonic mean of the precision and recall, the confusion matrix is an  $n \times n$  matrix by comparing the actual class of raw image and predicted class of classified image (Powers 2011; Chicco & Jurman 2020). Detailed procedures are demonstrated in Figure 2.

### Imagery pre-processing for GIS

Image pre-processing is the critical step in remote sensing applications. Many commercial software packages like ArcGIS and MapInfo have mature techniques and associated functions to process images for different industries and issues. The remote sensing data processing includes geometric referencing, image fusion, image mosaic, image cropping, cloud removal, shadow processing and atmospheric correction (Camps-Valls *et al.* 2011; Yang & Li 2015).

The focus of remote sensing image pre-processing is diverse to the different application requirements of various industries. For example, atmospheric correction is an essential process for remote sensing-based agricultural management that reduces

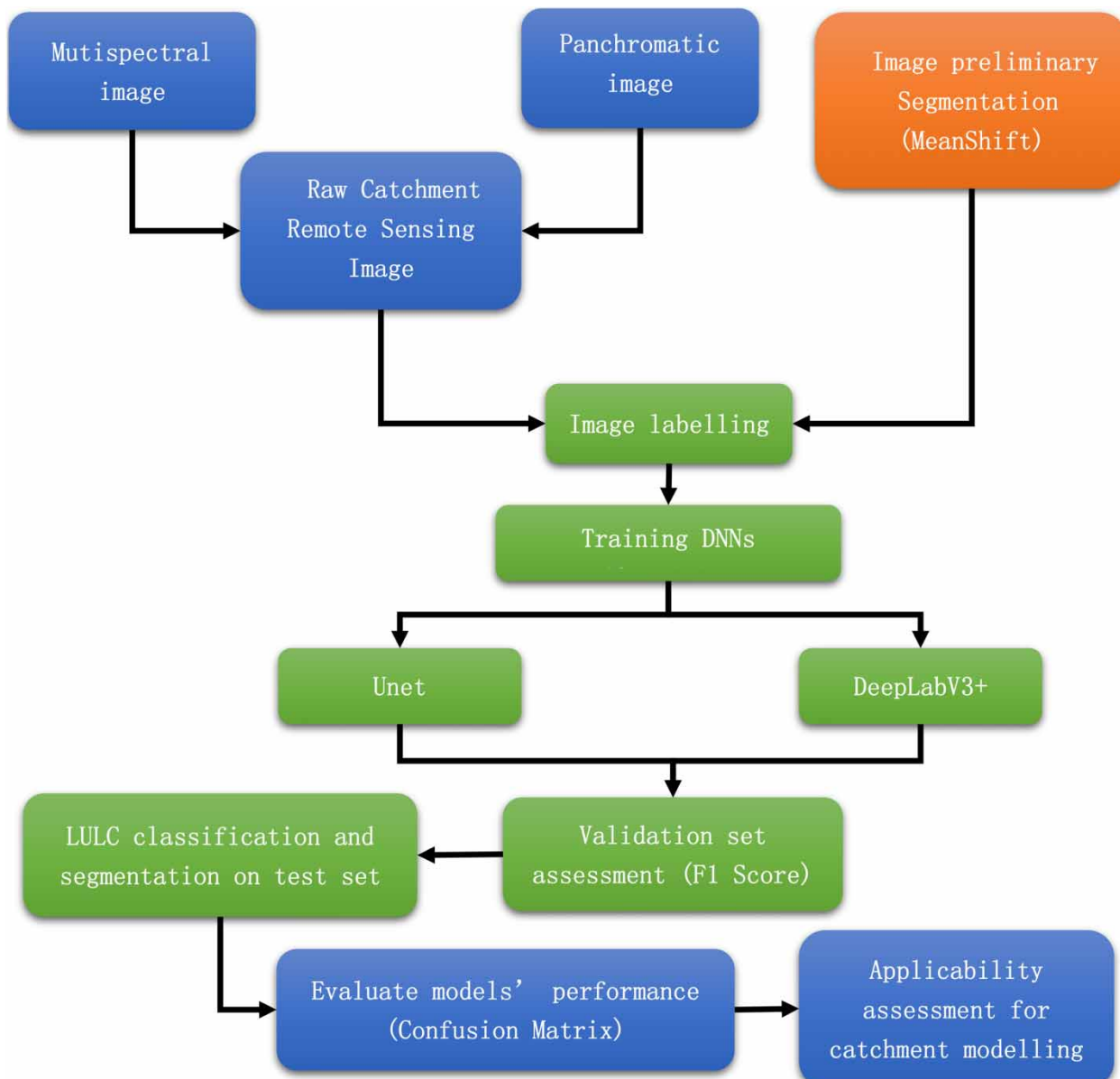


**Figure 2** | Flowchart of LULC extraction procedures proposed by this study.



the impact of atmospheric scattering and clouds obstruction on images (Wu *et al.* 2005). Regarding catchment modelling, the focus is on LULC recognition and geometric accuracy, which requires high image resolution and geometric correction. Therefore, it is necessary to process the image fusion by using the panchromatic image as the reference image to register the multi-spectral image to obtain the RGB remote sensing images with geographic coordinates and high resolution (Thomas *et al.* 2008; Bai *et al.* 2015; Ghassemian 2016).

High-resolution remote sensing imagery for the catchment in 2019 was collected from MapServer (Spatial Services of New South Wales Government), with three bands (Red, Green and Blue) and a resolution of  $25,344 \times 20,992$  (0.29 m/pixel width) (NSW Spatial Service 2021). The coordinate system of source imagery is WGS 84/UTM zone 56S. A digital surface model (DSM) was utilised as the base layer for the treatment of multi-spectral image orthorectification and thereafter to geometrically correct the image to ensure it was planimetrically projected. The GIS platform ArcGIS Pro Version 2.8.2 was applied to delineate the catchment vector boundary. Following these steps, the catchment boundary was used to clip the remote sensing imagery and unify the geocoordinate system.

### Training sample generation

In machine learning, a common approach is to use a large number of task-related data sets to:

- train the model,
- adjust the model's parameters through the continuous iteration of training error on the data sets and
- get the optimised model that best fits the model data set.

This is also referred to as supervised learning (Hastie *et al.* 2009). The construction of the training set requires a large number of labelled data (pictures, text files, videos, etc.) to provide a mapping channel for the model training. In the CV field, data labelling is used to identify the original images or videos and add one or more meaningful labels, which objectively establishes a mapping channel from data to results for the machine learning model to learn information from it (Cowie *et al.* 2011). For example, in the task of LULC recognition of remote sensing images, the label can be the binary representation of an object within an image, or it can be the semantic delineation of ground surface features at the pixel level. The starting point for data labelling requires humans to make judgments on designated unlabelled data. The trained model can be applied to make predictions on new data sets by learning hidden patterns within the human ascribed labels (Li *et al.* 2021). Labels are treated as objective criteria to train and evaluate the supervised machine learning model, often referred to as a 'standard answer'. The model training and accuracy of the prediction depends on the correctness of the 'standard answer', so it is essential to allocate sufficient time and resources for labelling to ensure the high accuracy of labels.

The ratio of the training and validation was set to 9:1. The trained model will be applied to make predictions on the entire catchment imagery (Figure 3) for testing the model's performance on the rest area of the imagery without labels. In catchment modelling systems, the determination of representative class schema depends on the comprehensive land-cover conditions and the catchment spatial features that affect the catchment rainfall-runoff process. Therefore, I defined the catchment LULC class schema for this study as roof, road, railway, water, impervious, pervious and tree by referring to the zoning map from the City of Sydney Council and observable features of the catchment remote sensing imagery. The manual labelling approach was used to maintain the accuracy and consistency of label masks. It is worth mentioning that some ground surface features are occluded by the tree canopies, which leads to identification difficulties and incorrect labelling. To address this issue, I ignored the occluded ground features but delineated and labelled the tree canopies above them to ensure the stability of the mapping channel. The tree can be seen as an uncertainty class, where its prediction should be analysed with other conditions to obtain the correct parameter for catchment modelling purposes. Approximately 25% of the image area was labelled. An image clipping tool was applied to grid the labelled area into 5,636 small images with a size of  $256 \times 256$  and then rasterise them to generate the label masks by snapping to the pixel alignment. Figure 3 shows the labelling area and class schema of the study.

### MeanShift for image pre-segmentation

The MeanShift image segmentation algorithm extracts general information from the complex features through coarsening and then segmenting the image (Comaniciu & Meer 2002). The concept of MeanShift was first proposed by Fukunaga & Hostetler (1975). In unsupervised learning, MeanShift refers to a density-based non-parametric clustering algorithm that assumes the data of different clusters conform to the corresponding probability density distributions and finds the density

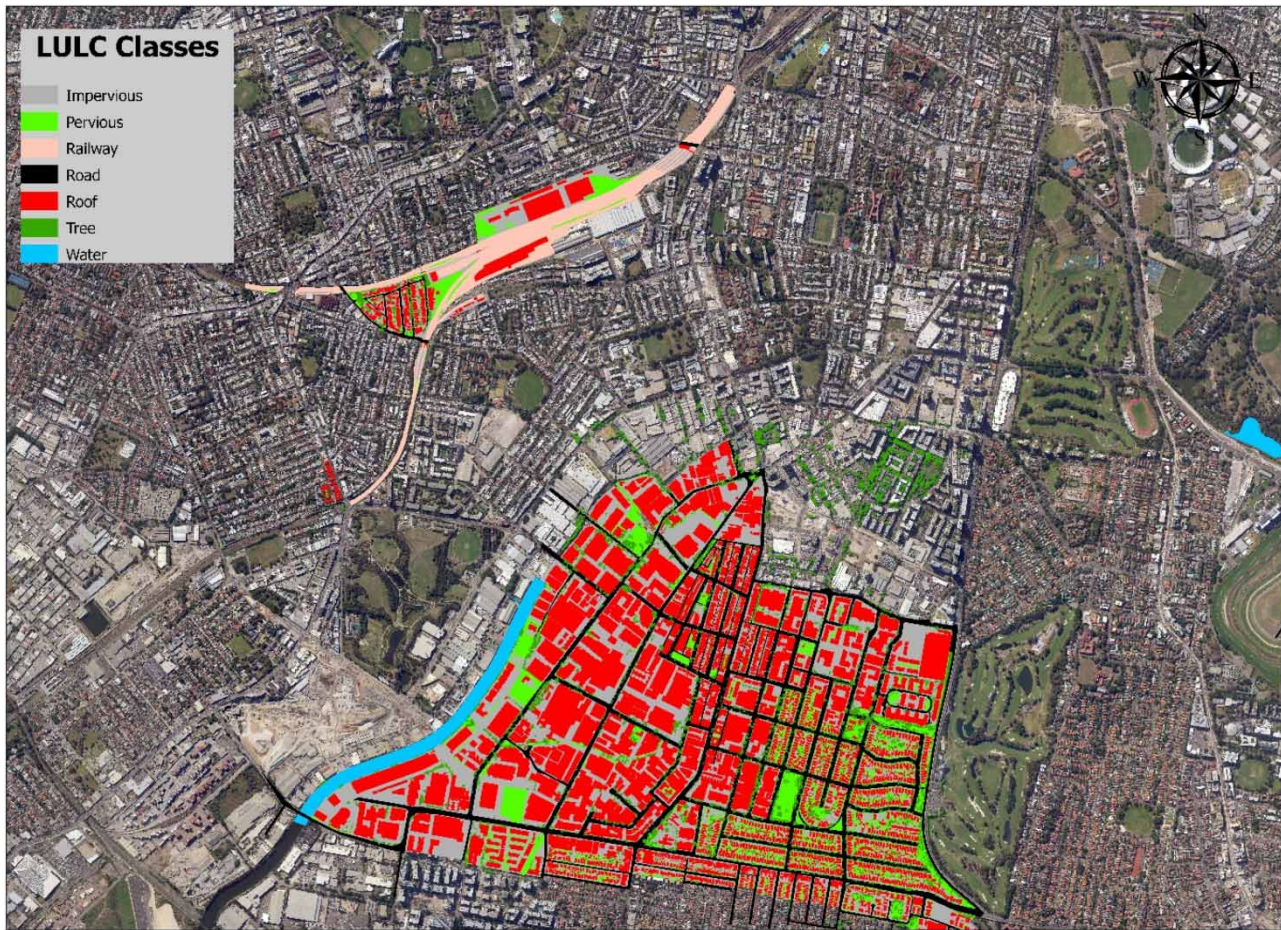


**Figure 3** | Class representatives and labels of the study catchment.

vector of any sample points in which the highest vector means the direction of iterations. These sample points will eventually converge to the area with the maximum local density, and the points that converge to the same local maximum are considered members of the same cluster (Comaniciu & Meer 2002; Szeliski 2010). In image segmentation, MeanShift can be used to segment image objects by clustering the neighbouring pixels with similar spectral and texture information.

Pixels of remote sensing imagery usually contain two types of information: coordinate information and colour information, which constitute the spatial features of the image (Foley *et al.* 1994). In the urbanised Alexandria Canal catchment, the regular geometric of artificial structures and the similar colours of vegetation lay the foundation for the use of MeanShift for preliminary image segmentation. In addition, the spatial features of the imagery are very complex, and the associated data amount is enormous due to the high heterogeneity of the catchment LULC. Therefore, it is necessary to take preliminary segmentation measures to simplify the spatial features of the image. In this study, the MeanShift segmentation result was used as the input of the DNN classifier to train the model and test set to make predictions of LULC. Figure 4 shows the examples of segmentation by MeanShift.

### Deep learning for image classification and segmentation

Two deep neural network-based algorithms, such as U-net and DeepLabV3+, were selected to conduct the study catchment's LULC classification and semantic segmentation. In the distributed catchment modelling systems, any catchment's internal spatial characteristics and distribution that affect the rainfall-runoff process should be considered and parameterised, where the spatial patterns are expressed by pixel in remote sensing imagery. Therefore, the pixel-based semantic segmentation methods were chosen instead of the object focused instance segmentation method.



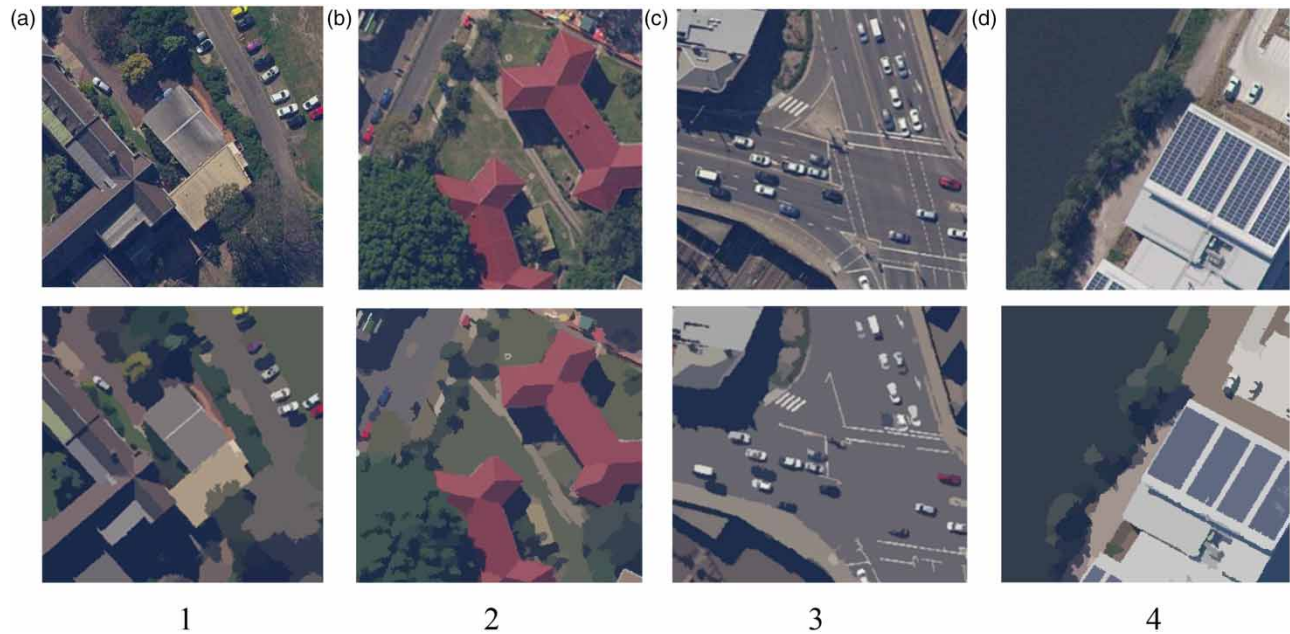


**Figure 4** | Raw images (a–d) and their MeanShift segmentation (1, 2, 3, 4).

### U-Net

U-Net is one of the earliest algorithms for semantic segmentation using fully convolutional networks (Ronneberger *et al.* 2015). The proposed symmetrical U-shaped structure with innovative encoding and decoding paths has affected the development of many segmentation networks such as U-net++ (Zhou *et al.* 2018) and SegNet (Badrinarayanan *et al.* 2017).

In this study, the pre-trained model Resnet-34 was applied as the backbone for enhancing the downsampling process. A schematic diagram of U-net with the pre-trained backbone neural network ResNet-34 (He *et al.* 2016) is demonstrated in Figure 5.

The left side of the network is a series of downsampling operations composed of four convolution and max-pooling layers, and the right side of the network is called the expansive path with four upsampling layers to recover the feature map to its

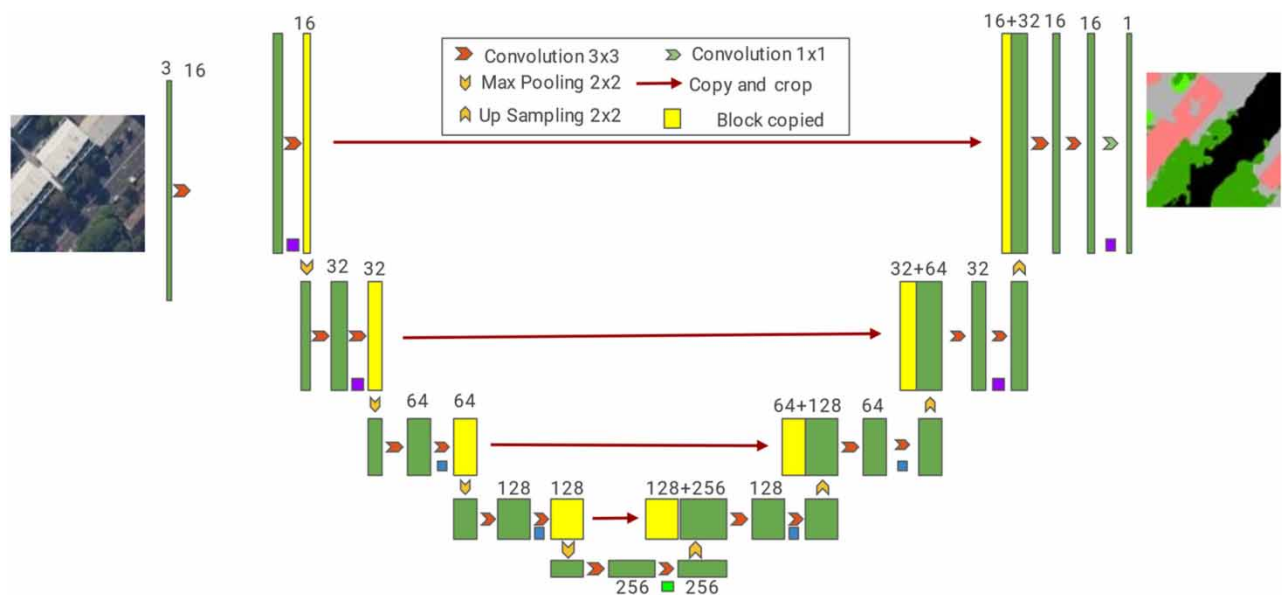


**Figure 5** | Framework of U-net architecture with Resnet-34 for downsampling.



original resolution. The upsampling outputs are connected to the corresponding cropped feature maps from the downsampling path, where the features learned during downsampling are applied to the upsampling to enhance the accuracy of output.

### DeepLabV3+

DeepLabV3+ is the fourth generation of the DeepLab series of semantic segmentation models developed by Google, with encoder-decoder architecture, which is different from the progressive upsampling of the classic symmetric neural networks (e.g. U-net). DeepLab uses atrous convolution to reduce the downsampling rate without losing the receptive field, that the final feature map contains rich and elaborate semantics information. The original resolution can be restored directly through interpolation instead of the downsampling feature maps' horizontal connection (Chen *et al.* 2018).

The architecture of DeepLabV3+ is shown in Figure 6. The main body encoder part is a deep convolutional neural network (DCNN) with atrous convolution, the commonly used DCNN such as ResNet can be used, followed by the Atrous Spatial Pyramid Pooling module (ASPP) for introducing multi-scale information. DeepLabV3+ introduced the decoder part to improve the segmentation accuracy of class boundary by integrating the features of different levels.

### Accuracy assessment

A typical evaluation index of classification performance is accuracy, which can directly reflect the percentage of correct classification. However, in the semantic classification of urban remote sensing imagery, the percentages of each LULC class are not uniformly distributed, which lead to the evaluation bias to the big class with a large area if there is no adjustment to balance the data set. The  $\kappa$  coefficient (Stehman 1996), an index that can punish the 'bias' of the model, is needed to replace a pure accuracy assessment. A robust model appreciates a higher  $\kappa$  coefficient, scilicet a balanced confusion matrix reflects a higher  $\kappa$  coefficient, vice versa. The expression of  $\kappa$  coefficient is as follows:

$$\kappa = \frac{p_o - p_e}{1 - p_e}$$

where  $p_o$  is the sum of all observed correct classification, and  $p_e$  is the hypothetical probability of each class, using the classified data to calculate the probabilities of each class from the view of users (Sim & Wright 2005).

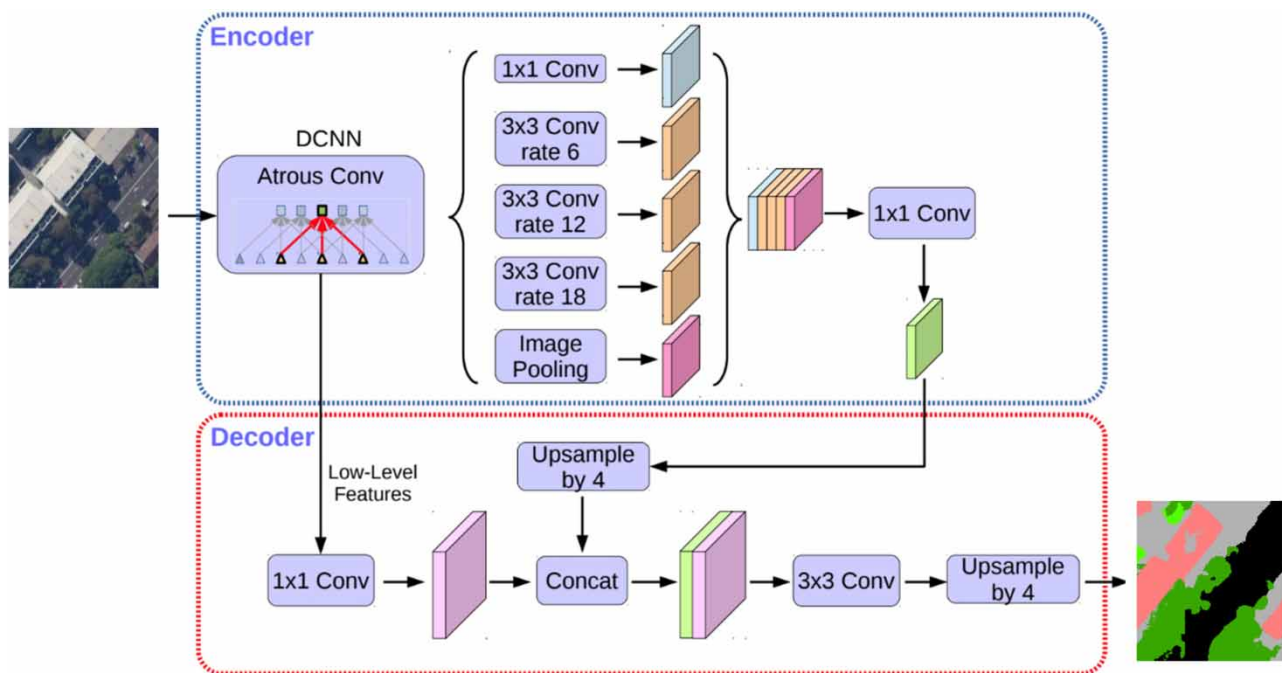


**Figure 6** | Architecture of DeepLabV3+ (Chen *et al.* 2018).

In this study, the stratified random method was applied to create 500 assessment points that are randomly distributed in each class. The number of points in each class is proportional to its class area. Then, the  $\kappa$  coefficient was calculated by confusion matrix to evaluate the prediction consistency.

## RESULTS AND DISCUSSION

### Model training and prediction

In this study, three methods were used to predict LULC from remote sensing images of the study catchment, namely U-net, DeepLabV3+ and MeanShift+U-net, with the same test set, training set amounts and masks. The pre-trained backbone neural network and iteration parameter was set to Resnet-34 and 50 for all three methods. The difference is that the MeanShift+U-net method uses the preliminary segmented imagery as the base map instead of the raw images adopted by the other two methods. Figure 7 shows the training and validation loss curves. The training process of the three models was smooth, and the fast convergence of the loss was achieved, which indicates that the gradient is continuously decreasing and the selected learning rate is appropriate. U-net has the best training performance, followed by MeanShift+U-net, and the last one is DeepLabV3+. A vibration occurred on the verification curve of DeepLabV3+, and the fitting degree between the verification and training is not as good as the former two. Figure 8 shows the performance of the three methods on the verification set.

The  $f1$  score is involved to evaluate the model's performance in terms of prediction accuracy. The  $F1$  score is an index used in statistics to measure the accuracy of a two-class model considering both the precision and recall of the classification model,

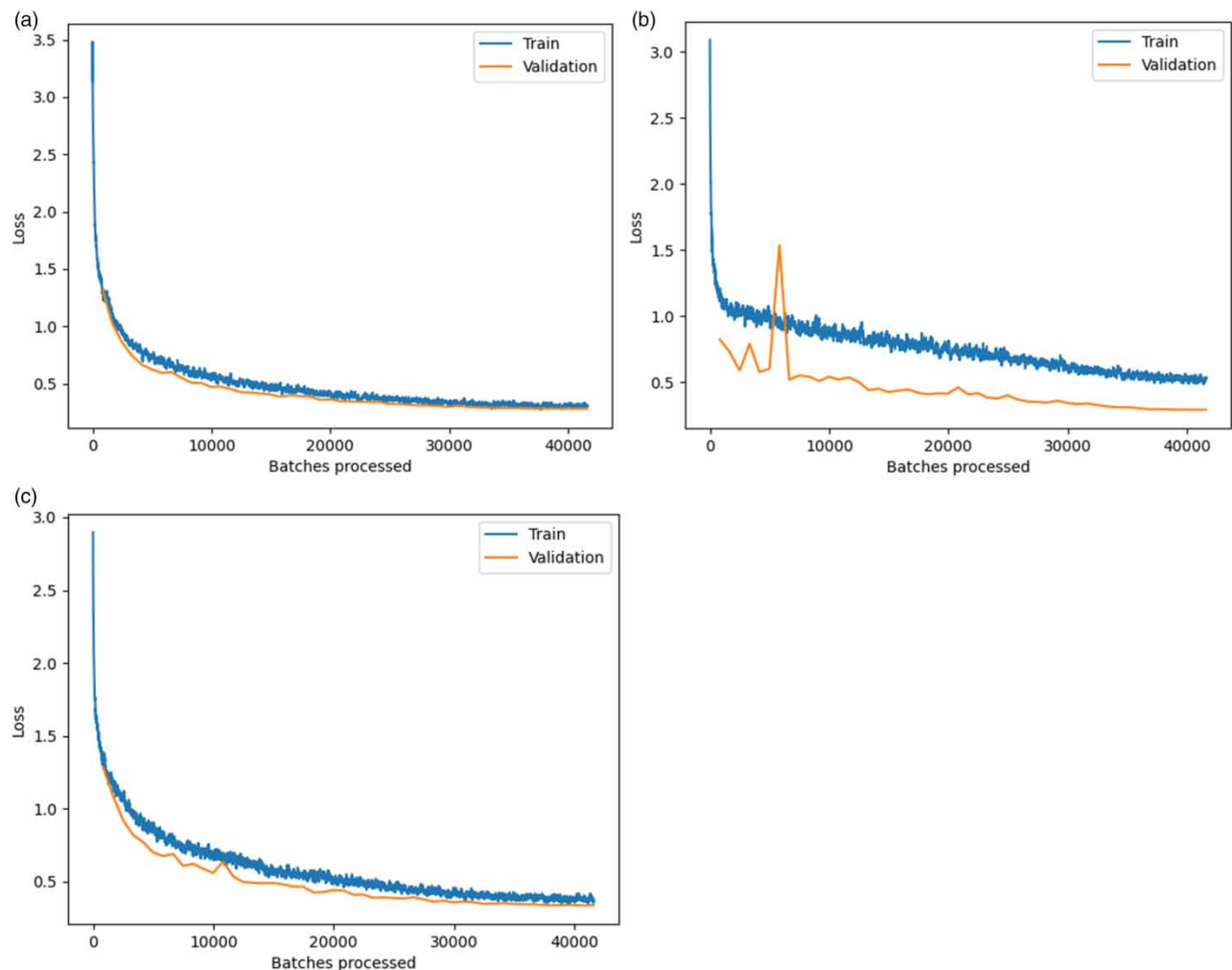


**Figure 7** | Training and validation loss curves of (a) U-net, (b) DeepLabV3+ and (c) MeanShift+U-net.

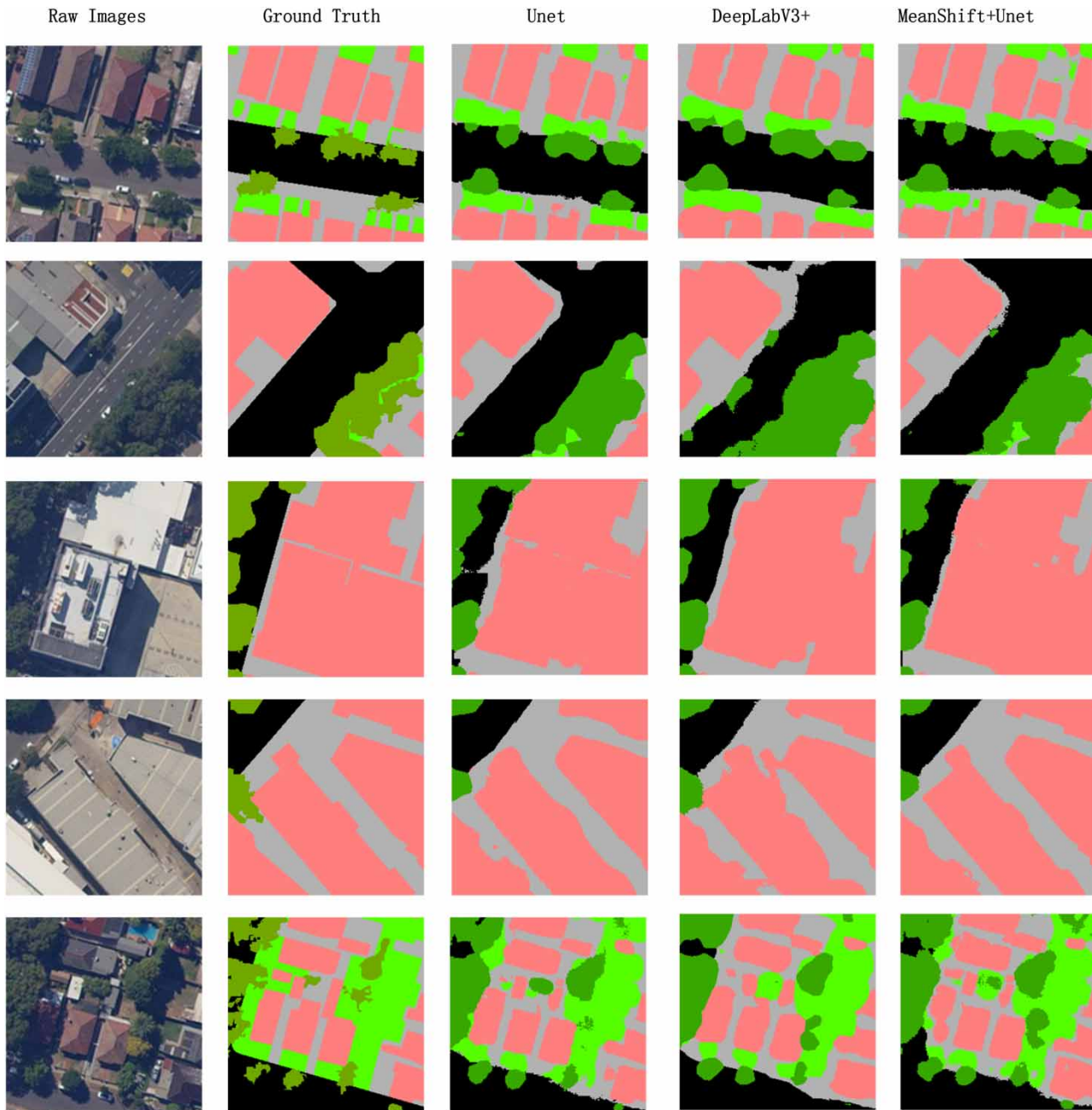


**Figure 8** | Illustration of LULC segmentation on the validation set.

which can be regarded as a harmonic average of the model's precision and recall (Powers 2011; Tharwat 2020). The equation of the  $F1$  score is as follows:

$$F1 = \frac{2}{\text{Recall}^{-1} + \text{Precision}^{-1}}$$

The advantage of the  $F1$  score is avoiding the unstable recall and precision due to the excessive number of positive samples. Figure 9 shows the  $F1$  score of three models in each class. The three methods have minor differences in the  $F1$  scores of each LULC class. U-net performs better in major classes (e.g. roof and impervious), and DeeplabV3+ performs better in minor classes (e.g. tree and road), which may be powered by its excellent boundary segmentation capability. The overall



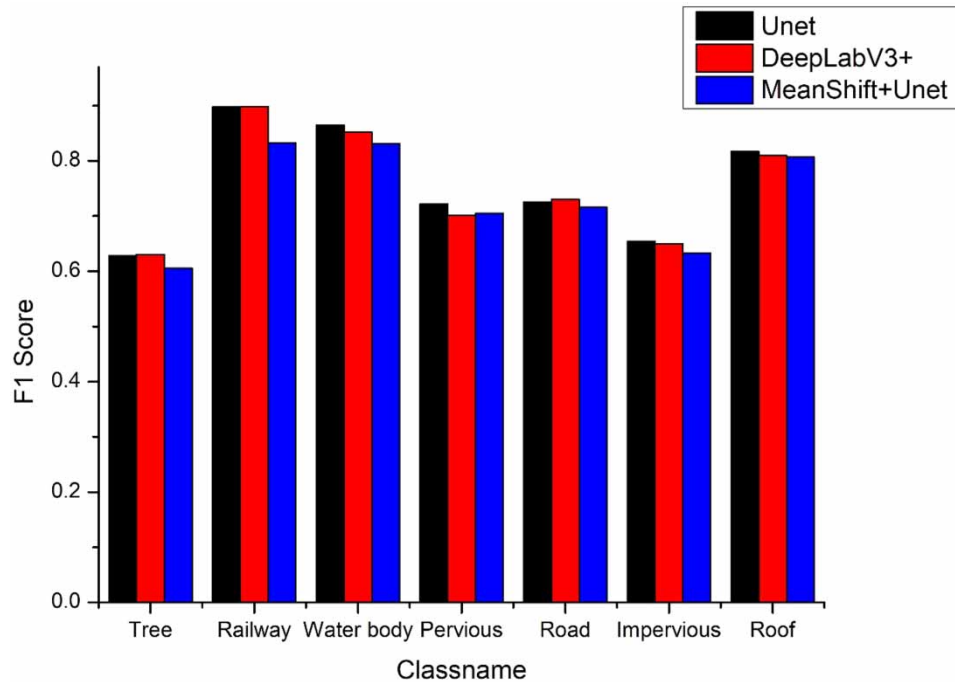


**Figure 9** | F1 score of U-net, DeepLabV3+ and MeanShift+U-net in each class.

performance of MeanShift+U-net is lower than the other two methods, but the prediction is more balanced, which means better consistency between input and output.

### Confusion matrix and $\kappa$ coefficient

In the performance evaluation strategy, the confusion matrix and the  $\kappa$  coefficient were applied to assess the performance of the three trained models in predicting the LULC of the study catchment.

Five hundred random points were created on the catchment imagery as assessment points, where the number of points in each class is proportional to its corresponding area percentage.

The  $\kappa$  coefficient for all three trained models exceeded 0.75; the  $\kappa$  coefficient values are 0.7929, 0.7593 and 0.7955 for U-net, DeepLabV3+ and MeanShift+U-net, respectively. These  $\kappa$  coefficients indicate that the classification results of the three trained models are strongly consistent, and there is no bias towards the major classes with large areas. The U\_Accuracy and P\_Accuracy represent the User Accuracy and Prediction Accuracy for reflecting the model's accuracy from different observation channels. For example, in the tree class of Table 1, 16 points lost the correctness among the total 72 assessing points, and 56 points were counted to the correct class within 65 classified samples so that the P\_Accuracy and U\_Accuracy are 0.7778 and 0.8615. Tables 1–3 show the confusion matrixes and  $\kappa$  coefficients of the three trained models.

### Discussion for catchment modelling

This section will discuss the suitability of the test results of the above three methods in two types of catchment modelling systems (fully-distributed and semi-distributed modelling systems). Both fully-distributed and semi-distributed models involve considering catchment spatial pattern distribution when determining the runoff generation and routing, where the remote sensing datasets such as imagery and DEM are widely applied in obtaining spatial features for modelling purposes (Bell *et al.* 2009; Ball *et al.* 2019).

The remote sensing-based catchment modelling systems have rigorous requirements for the geometric accuracy of spatial features in estimating the model's parameters. Therefore, the selected index of suitability assessment for catchment modelling should be the P\_Accuracy (Prediction Accuracy) values of the CV model on the test set, which can reflect the classification and segmentation correctness of the CV model on each LULC class. Tables 1–3 illustrate that the three methods' overall prediction accuracy values have all exceeded 0.8, yielding 0.8360, 0.8103 and 0.8379 for U-net, DeepLabV3+ and MeanShift+U-net, respectively. In addition, the  $\kappa$  coefficient of MeanShift+U-net is the highest among the three methods, which means

**Table 1** | Confusion matrix of the classification results achieved by U-net

| Classname  | Tree   | Railway | Water body | Pervious | Road   | Impervious | Roof   | Total | U_Accuracy |
|------------|--------|---------|------------|----------|--------|------------|--------|-------|------------|
| Tree       | 56     | 0       | 0          | 7        | 0      | 1          | 1      | 65    | 0.8615     |
| Railway    | 0      | 7       | 0          | 0        | 2      | 1          | 0      | 10    | 0.7000     |
| water Body | 2      | 0       | 8          | 0        | 0      | 0          | 0      | 10    | 0.8000     |
| Pervious   | 7      | 0       | 1          | 66       | 0      | 3          | 0      | 77    | 0.8571     |
| Road       | 3      | 0       | 0          | 0        | 57     | 3          | 0      | 63    | 0.9048     |
| Impervious | 4      | 0       | 0          | 24       | 8      | 79         | 11     | 126   | 0.6270     |
| Roof       | 0      | 0       | 0          | 0        | 0      | 5          | 150    | 155   | 0.9677     |
| Total      | 72     | 7       | 9          | 97       | 67     | 92         | 162    | 506   |            |
| P_Accuracy | 0.7778 | 1       | 0.8889     | 0.6804   | 0.8507 | 0.8587     | 0.9259 |       | 0.8360     |

P\_Accuracy = Prediction Accuracy; U\_Accuracy = User Accuracy.

Overall accuracy = 0.8360;  $\kappa$  = 0.7929.

**Table 2** | Confusion matrix of the classification results achieved by DeepLabV3+

| Classname  | Tree   | Railway | Water body | Pervious | Road   | Impervious | Roof   | Total | U_Accuracy |
|------------|--------|---------|------------|----------|--------|------------|--------|-------|------------|
| Tree       | 56     | 0       | 0          | 3        | 4      | 2          | 0      | 65    | 0.8615     |
| Railway    | 0      | 6       | 0          | 0        | 0      | 1          | 0      | 7     | 0.8571     |
| Water body | 2      | 0       | 9          | 1        | 0      | 0          | 0      | 12    | 0.7500     |
| Pervious   | 6      | 0       | 0          | 67       | 0      | 5          | 1      | 79    | 0.8481     |
| Road       | 1      | 0       | 0          | 2        | 55     | 1          | 0      | 59    | 0.9322     |
| Impervious | 7      | 0       | 0          | 21       | 4      | 71         | 15     | 118   | 0.6017     |
| Roof       | 0      | 1       | 0          | 3        | 4      | 12         | 146    | 166   | 0.8795     |
| Total      | 72     | 7       | 9          | 97       | 67     | 92         | 162    | 506   | 0          |
| P_Accuracy | 0.7778 | 0.8571  | 1          | 0.6907   | 0.8209 | 0.7717     | 0.9012 |       | 0.8103     |

P\_Accuracy = Prediction Accuracy; U\_Accuracy = User Accuracy.

Overall accuracy = 0.8103;  $\kappa$  = 0.7593.

**Table 3** | Confusion matrix of the classification results achieved by MeanShift+U-net

| Classname  | Tree   | Railway | Water body | Pervious | Road   | Impervious | Roof   | Total | U_Accuracy |
|------------|--------|---------|------------|----------|--------|------------|--------|-------|------------|
| Tree       | 56     | 0       | 0          | 7        | 0      | 1          | 1      | 65    | 0.8615     |
| Railway    | 0      | 7       | 0          | 0        | 2      | 1          | 0      | 10    | 0.700      |
| Water body | 2      | 0       | 8          | 0        | 0      | 0          | 0      | 10    | 0.800      |
| Pervious   | 7      | 0       | 1          | 66       | 0      | 3          | 0      | 77    | 0.8571     |
| Road       | 3      | 0       | 0          | 0        | 57     | 3          | 0      | 63    | 0.9048     |
| Impervious | 4      | 0       | 0          | 24       | 8      | 80         | 11     | 127   | 0.6299     |
| Roof       | 0      | 0       | 0          | 0        | 0      | 4          | 150    | 154   | 0.9740     |
| Total      | 72     | 7       | 9          | 97       | 67     | 92         | 162    | 506   |            |
| P_Accuracy | 0.7778 | 1       | 0.8889     | 0.6804   | 0.8507 | 0.8695     | 0.9259 |       | 0.8379     |

P\_Accuracy = Prediction Accuracy; U\_Accuracy = User Accuracy.

Overall accuracy = 0.8379;  $\kappa$  = 0.7955.

MeanShift+U-net has the best consistency in predicting the LULC of the catchment. The advantage of consistency will be gradually expanded with the increase of the prediction area, which is beneficial to maintaining the stability and robustness of the parameter estimation model under the changing catchment conditions. Therefore, the MeanShift+U-net method

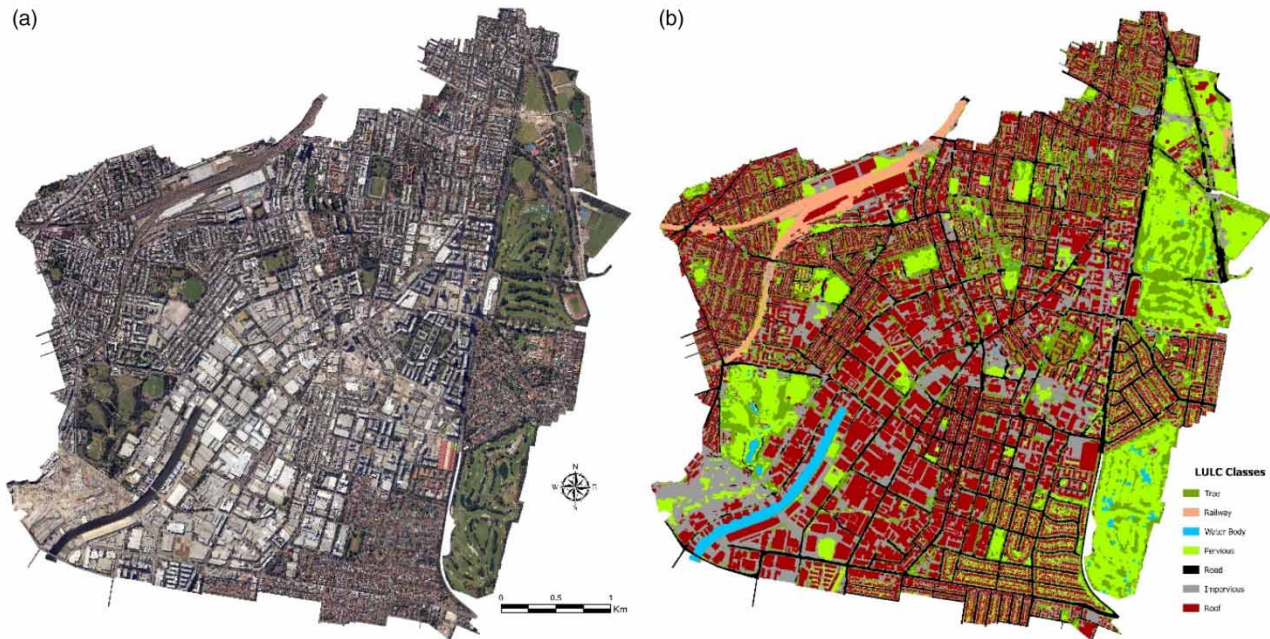


**Figure 10** | Alexandria Canal catchment raw image (a) and MeanShift+U-net prediction of LULC (b).

has the best performance in extracting LULC information at the pixel scale among the three with the overall P\_accuracy of 0.8379. Figure 10 shows the MeanShift+U-net LULC prediction of the entire catchment.

MeanShift+U-net prediction is also tested at the subcatchment scale under the schema of semi-distributed modelling systems, which have a pre-determined flow direction and the requirement of fewer parameters. The spatial distribution is ignored within the subcatchment scale of the semi-distributed model (Sitterson *et al.* 2018). For example, Choi & Ball (2002) categorised the control parameters of the SWMM into measured and inferred parameters, where the inferred parameters such as impervious ratio, subcatchment length/width, depression storage, infiltration and Manning's roughness coefficients are highly related to the classification result and segmentation geometry of catchment LULC expected to be obtained from the MeanShift+U-net prediction. Therefore, the original four sub-classes (railway, road, impervious and roof) treated as the impervious feature were merged into one class (Impervious) in the confusion matrix. The new class schema is 'Tree', 'Pervious', 'Waterbody' and 'Impervious'. The purpose of this simplified class schema is to assess the suitability of the semi-distributed modelling systems by ignoring the classification errors among the sub-classes with impervious rainfall responses. Tables 4 and 5 show the confusion matrixes of the DeepLabV3+, U-net and MeanShift+U-net after merging classes. One table (Table 5) is used to show the simplified confusion matrix for both U-net and MeanShift+U-net due to their same accuracy distribution among the 500 assessing points. The P\_Accuracy value of 'Impervious' was significantly increased in the three methods under the simplified class schema, in which the 'Impervious' P\_Accuracy occurred from U-net,

**Table 4** | Confusion matrix of DeepLabV3+ after merging classes

| ClassValue | Tree   | Water body | Pervious | Impervious | Total | U_Accuracy |
|------------|--------|------------|----------|------------|-------|------------|
| Tree       | 56     | 0          | 3        | 6          | 65    | 0.8615     |
| Water body | 2      | 9          | 1        | 0          | 12    | 0.75       |
| Pervious   | 6      | 0          | 67       | 6          | 79    | 0.8481     |
| Impervious | 8      | 0          | 26       | 316        | 350   | 0.9028     |
| Total      | 72     | 9          | 97       | 328        | 506   |            |
| P_Accuracy | 0.7778 | 1          | 0.6907   | 0.9634     |       |            |

P\_Accuracy = Prediction Accuracy; U\_Accuracy = User Accuracy.

Overall accuracy = 0.8854;  $\kappa$  = 0.7721.



**Table 5** | Confusion matrix of U-net and MeanShift+U-net after merging classes

| ClassValue | Tree   | Water body | Pervious | Impervious | Total | U_Accuracy |
|------------|--------|------------|----------|------------|-------|------------|
| Tree       | 56     | 0          | 7        | 2          | 65    | 0.8615     |
| Water body | 2      | 8          | 0        | 0          | 10    | 0.8000     |
| Pervious   | 7      | 1          | 66       | 3          | 77    | 0.8571     |
| Impervious | 7      | 0          | 24       | 323        | 354   | 0.9124     |
| Total      | 72     | 9          | 97       | 328        | 506   |            |
| P_Accuracy | 0.7778 | 0.8889     | 0.6804   | 0.9847     |       |            |

P\_Accuracy = Prediction Accuracy; U\_Accuracy = User Accuracy.

Overall accuracy = 0.8953;  $\kappa$  = 0.7900.

MeanShift+U-net and DeepLabV3+ are 0.9847, 0.9847 and 0.9634, respectively. The  $\kappa$  coefficient of DeepLabV3+ has been improved but is still lower than the other two methods.

Considering the highest  $\kappa$  coefficient achieved by MeanShift+U-net in the original class schema, MeanShift+U-net is recommended for estimating the initial parameters of semi-distributed modelling systems. Reasons are as follows: First of all, the semi-distributed model does not require high geometric accuracy of the spatial features within the subcatchment scale, which reduce the probability of models' failure by downgrading the resolution of prediction error. Secondly, the estimated parameters for the semi-distributed model are more accurate as the impervious area prediction accuracy (0.9847) of MeanShift+U-net is very close to the accuracy of manual delineation. In addition, the parameter uncertainty caused by the CV model error is objectively reduced since the number of parameters of the semi-distributed model is much less than that of the fully distributed model. Finally, the higher  $\kappa$  coefficient of the MeanShift+U-net method illustrates that its better classification consistency could maintain a stable prediction accuracy on the sizeable urban catchment with high heterogeneity of LULC. However, the number of subcatchments in a metropolis could be very large due to the complex LULC and drainage system-controlled land divisions. In the specific implementation of MeanShift+U-net on catchment parameterisation, it is necessary to simplify the large number of subcatchments to a certain extent to reduce the impact of the error caused by the high resolution of spatial features.

Nevertheless, this method still has some significant drawbacks as follows:

- There is a significant gap in achieving accurate geometric parameters of the catchment spatial features at the pixel scale by referring to the overall P\_Accuracy. This error will be gradually enlarged, with the expansion of the study catchment area, and causes the collapse of the entire model eventually.
- The occlusion of tree canopy and buildings' shadows could lead to incorrect determinations of the underlying ground features. Further study about mitigation approaches is necessary to reduce their negative effect.
- The spectral similarity between the bare soil and the impervious area, resulting in a large portion of bare soil with pervious rainfall response was classified as an impervious feature, which will further lead to the uncertainty of the parameters and the instability of the catchment model.
- Errors and misprediction could occur when using these approaches on other remote sensing databases such as Google and Quickbird due to the pixel spectral variation caused by different image processing methods.

It is recommended to train the deep learning models on the associated remote sensing dataset before applying the approach to a practical catchment model. The LULC class schema used in this study is not fixed. Modellers should set up suitable LULC classes to represent catchment spatial features and correlate to the catchment rainfall-runoff process.

## CONCLUSION

This paper proposes three methods for LULC classification on Alexandria Canal catchment remote sensing imagery. The study imagery was pre-processed, and the MeanShift algorithm was applied to achieve preliminary segmentation of the catchment LULC objects with similar spatial features. The raw catchment image samples were trained using U-net and DeepLabV3+, and the MeanShift+U-net was trained by the pre-segmented catchment image of MeanShift. Then, the U-net, DeepLabV3+ and MeanShift+U-net worked as the classifier for the study catchment imagery. Finally, the confusion matrix was applied to assessing the suitability of the prediction for catchment modelling systems.

In contrast with the pure U-net and DeepLabV3+, MeanShift+U-net has achieved the best prediction accuracy and excellent consistency in the study catchment. Both original and simplified confusion matrices indicate that the proposed methods are more applicable to estimating spatial parameters for the semi-distributed catchment modelling systems, where the MeanShift+U-net is recommended due to its high accuracy (0.9847) in classifying impervious features. (In addition, it is necessary to explore the performance of MeanShift+U-net on multi-sources remote sensing dataset and evaluate its consistency on different LULC classes further, as well as the influence of image noise such as tree canopy and buildings' shadow on the classification accuracy, so as to improve the method's practicality in the catchment modelling field.)

## ACKNOWLEDGEMENTS

The land zoning map, drainage network and cadastral map of the Alexandria Canal catchment are provided by the City of Sydney Council, Sydney, Australia. Sincere thanks are given for the support of the City of Sydney Council and their flood risk management team.

## DATA AVAILABILITY STATEMENT

Data cannot be made publicly available; readers should contact the corresponding author for details.

## REFERENCES

- Abulohom, M., Shah, S. & Ghumman, A. 2001 *Development of a rainfall-runoff model, its calibration and validation*. *Water Resources Management* **15** (3), 149–163.
- Arnold Jr., C. L. & Gibbons, C. J. 1996 *Impervious surface coverage: the emergence of a key environmental indicator*. *Journal of the American Planning Association* **62** (2), 243–258.
- Badrinarayanan, V., Kendall, A. & Cipolla, R. 2017 *SegNet: a deep convolutional encoder-decoder architecture for image segmentation*. *IEEE Transactions on Pattern Analysis and Machine Intelligence* **39** (12), 2481–2495.
- Bai, L., Xu, C. & Wang, C. 2015 *A review of fusion methods of multi-spectral image*. *Optik* **126** (24), 4804–4807.
- Ball, J., Babister, M., Nathan, R., Weinmann, P., Weeks, W., Retallick, M. & Testoni, I. 2019 *Australian Rainfall and Runoff – A Guide to Flood Estimation*. Commonwealth of Australia (Geoscience Australia), Canberra.
- Bell, V., Kay, A., Jones, R., Moore, R. & Reynard, N. 2009 *Use of soil data in a grid-based hydrological model to estimate spatial variation in changing flood risk across the UK*. *Journal of Hydrology* **377** (3–4), 335–350.
- Beven, K. J. 2012 *Rainfall-Runoff Modelling: The Primer*, 2nd edn. Wiley Blackwell, Chichester.
- Boegh, E., Thorsen, M., Butts, M., Hansen, S., Christiansen, J., Abrahamsen, P., Hasager, C., Jensen, N. O., van der Keur, P. & Refsgaard, J. C. 2004 *Incorporating remote sensing data in physically based distributed agro-hydrological modelling*. *Journal of Hydrology* **287** (1–4), 279–299.
- Camps-Valls, G., Tuia, D., Gómez-Chova, L., Jiménez, S. & Malo, J. 2011 *Remote sensing image processing*. *Synthesis Lectures on Image, Video, and Multimedia Processing* **5** (1), 1–192.
- Chen, L.-C., Zhu, Y., Papandreou, G., Schroff, F. & Adam, H. 2018 *Encoder-decoder with atrous separable convolution for semantic image segmentation*. In: *Paper Presented at the Proceedings of the European Conference on Computer Vision (ECCV)*.
- Cheng, Y. 1995 *Mean shift, mode seeking, and clustering*. *IEEE Transactions on Pattern Analysis and Machine Intelligence* **17** (8), 790–799.
- Chicco, D. & Jurman, G. 2020 *The advantages of the Matthews correlation coefficient (MCC) over F1 score and accuracy in binary classification evaluation*. *BMC Genomics* **21** (1), 1–13.
- Choi, K.-S. & Ball, J. E. 2002 *Parameter estimation for urban runoff modelling*. *Urban Water* **4** (1), 31–41.
- Comaniciu, D. & Meer, P. 2002 *Mean shift: a robust approach toward feature space analysis*. *IEEE Transactions on Pattern Analysis and Machine Intelligence* **24** (5), 603–619.
- Cowie, R., Cox, C., Martin, J.-C., Batliner, A., Heylen, D. & Karpouzis, K. 2011 *Issues in data labelling*. In: *Emotion-oriented Systems*. Springer, Berlin, pp. 213–241.
- Dawson, R., Speight, L., Hall, J., Djordjevic, S., Savic, D. & Leandro, J. 2008 *Attribution of flood risk in urban areas*. *Journal of Hydroinformatics* **10** (4), 275–288.
- Esri 2021 *World imagery*. In: DigitalGlobe, GeoEye, i-cubed, USDA FSA, USGS, AEX, Getmapping, Aerogrid, IGN, IGP, Swisstopo, and the GIS User Community. <https://www.arcgis.com/home/item.html?id=10df2279f9684e4a9f6a7f08febac2a9>. Accessed 3 May 2021.
- Foley, J. D., Van Dam, A., Feiner, S. K., Hughes, J. F. & Phillips, R. L. 1994 *Introduction to Computer Graphics*, Vol. 55. Addison-Wesley Reading, Boston, MA.
- Foody, G. M. 2004 *Mapping land cover from remotely sensed imagery for input to hydrological models*. In: *Neural Networks for Hydrological Modelling*. Swets and Zeitlinger Lisse, London, pp. 269–289.
- Fukunaga, K. & Hostetler, L. 1975 *The estimation of the gradient of a density function, with applications in pattern recognition*. *IEEE Transactions on Information Theory* **21** (1), 32–40.

- Gan, T. Y., Dlamini, E. M. & Biftu, G. F. 1997 Effects of model complexity and structure, data quality, and objective functions on hydrologic modeling. *Journal of Hydrology* **192** (1–4), 81–103.
- Ghassemian, H. 2016 A review of remote sensing image fusion methods. *Information Fusion* **32**, 75–89.
- Grigorescu, S., Trasnea, B., Cocias, T. & Macesanu, G. 2020 A survey of deep learning techniques for autonomous driving. *Journal of Field Robotics* **37** (3), 362–386.
- Hastie, T., Tibshirani, R. & Friedman, J. 2009 Overview of supervised learning. In: *The Elements of Statistical Learning*. Springer, New York, pp. 9–41.
- He, K., Zhang, X., Ren, S. & Sun, J. 2016 Identity mappings in deep residual networks. In: *Paper Presented at the European Conference on Computer Vision*.
- He, K., Gkioxari, G., Dollár, P. & Girshick, R. 2017 Mask r-cnn. In: *Paper Presented at the Proceedings of the IEEE International Conference on Computer Vision*.
- Holman-Dodds, J. K., Bradley, A. A. & Potter, K. W. 2003 Evaluation of hydrologic benefits of infiltration based urban storm water management 1. *JAWRA – Journal of the American Water Resources Association* **39** (1), 205–215.
- Hu, T., Yang, J., Li, X. & Gong, P. 2016 Mapping urban land use by using landsat images and open social data. *Remote Sensing* **8** (2), 151.
- Huang, B., Zhao, B. & Song, Y. 2018 Urban land-use mapping using a deep convolutional neural network with high spatial resolution multi-spectral remote sensing imagery. *Remote Sensing of Environment* **214**, 73–86.
- Jha, A. K., Bloch, R. & Lamond, J. 2012 *Cities and Flooding: A Guide to Integrated Urban Flood Risk Management for the 21st Century*. The World Bank, Washington, DC.
- Klein, A. G. & Barnett, A. C. 2003 Validation of daily MODIS snow cover maps of the Upper Rio Grande River Basin for the 2000–2001 snow year. *Remote Sensing of Environment* **86** (2), 162–176.
- Li, H., Ding, L., Ren, M., Li, C. & Wang, H. 2017 Sponge city construction in China: a survey of the challenges and opportunities. *Water* **9** (9), 594.
- Li, K., Li, G., Wang, Y., Huang, Y., Liu, Z. & Wu, Z. 2021 CrowdRL: an end-to-end reinforcement learning framework for data labelling. In: *Paper Presented at the 2021 IEEE 37th International Conference on Data Engineering (ICDE)*.
- Liu, Y., Liu, X., Gao, S., Gong, L., Kang, C., Zhi, Y., Chi, G. & Shi, L. 2015 Social sensing: a new approach to understanding our socioeconomic environments. *Annals of the Association of American Geographers* **105** (3), 512–530.
- Mackay, D. S., Samanta, S., Nemani, R. R. & Band, L. E. 2003 Multi-objective parameter estimation for simulating canopy transpiration in forested watersheds. *Journal of Hydrology* **277** (3–4), 230–247.
- Niemi, T. J., Kokkonen, T., Sillanpää, N., Setälä, H. & Koivusalo, H. 2019 Automated urban rainfall-runoff model generation with detailed land cover and flow routing. *Journal of Hydrologic Engineering* **24** (5), 04019011.
- NSW Government Spatial Service 2021 *Historical, Aerial and Satellite Imagery*. Available from: [https://www.spatial.nsw.gov.au/products\\_and\\_services/aerial\\_and\\_historical\\_imagery](https://www.spatial.nsw.gov.au/products_and_services/aerial_and_historical_imagery).
- Parkhi, O. M., Vedaldi, A. & Zisserman, A. 2015 *Deep Face Recognition*.
- Peel, M. C. & McMahon, T. A. 2020 Historical development of rainfall-runoff modeling. *Wiley Interdisciplinary Reviews: Water* **7** (5), e1471.
- Powers, D. M. W. 2011 Evaluation: from precision, recall and F-measure to ROC, informedness, markedness and correlation. *Journal of Machine Learning Technologies* **2** (1), 37–63.
- Rezaee, M., Mahdianpari, M., Zhang, Y. & Salehi, B. 2018 Deep convolutional neural network for complex wetland classification using optical remote sensing imagery. *IEEE Journal of Selected Topics in Applied Earth Observations and Remote Sensing* **11** (9), 3030–3039.
- Ronneberger, O., Fischer, P. & Brox, T. 2015 U-net: convolutional networks for biomedical image segmentation. In: *Paper Presented at the International Conference on Medical Image Computing and Computer-Assisted Intervention*.
- Salvadore, E., Bronders, J. & Batelaan, O. 2015 Hydrological modelling of urbanized catchments: a review and future directions. *Journal of Hydrology* **529**, 62–81.
- Sim, J. & Wright, C. C. 2005 The kappa statistic in reliability studies: use, interpretation, and sample size requirements. *Physical Therapy* **85** (3), 257–268. doi:10.1093/ptj/85.3.257.
- Sitterson, J., Knights, C., Parmar, R., Wolfe, K., Avant, B. & Muche, M. 2018 *An Overview of Rainfall-Runoff Model Types*.
- Stehman, S. 1996 Estimating the kappa coefficient and its variance under stratified random sampling. *Photogrammetric Engineering and Remote Sensing* **62** (4), 401–407.
- Szeliski, R. 2010 *Computer Vision: Algorithms and Applications*. Springer Science & Business Media, Berlin.
- Tharwat, A. 2020 Classification assessment methods. *Applied Computing and Informatics* **17** (1), 168–192.
- Thomas, C., Ranchin, T., Wald, L. & Chanussot, J. 2008 Synthesis of multi-spectral images to high spatial resolution: a critical review of fusion methods based on remote sensing physics. *IEEE Transactions on GeoScience and Remote Sensing* **46** (5), 1301–1312.
- Voulodimos, A., Doulamis, N., Doulamis, A. & Protopapadakis, E. 2018 Deep learning for computer vision: a brief review. *Computational Intelligence and Neuroscience*. <https://www.hindawi.com/journals/cin/2018/7068349/>. Accessed 31 June 2021.
- Willner, S. N., Otto, C. & Levermann, A. 2018 Global economic response to river floods. *Nature Climate Change* **8** (7), 594–598.
- Wu, J., Wang, D. & Bauer, M. E. 2005 Image-based atmospheric correction of QuickBird imagery of Minnesota cropland. *Remote Sensing of Environment* **99** (3), 315–325.



- Wulder, M. A., Masek, J. G., Cohen, W. B., Loveland, T. R. & Woodcock, C. E. 2012 Opening the archive: how free data has enabled the science and monitoring promise of Landsat. *Remote Sensing of Environment* **122**, 2–10.
- Yang, J. & Li, P. 2015 Impervious surface extraction in urban areas from high spatial resolution imagery using linear spectral unmixing. *Remote Sensing Applications: Society and Environment* **1**, 61–71.
- Zaman, M. A., Rahman, A. & Haddad, K. 2012 Regional flood frequency analysis in arid regions: a case study for Australia. *Journal of Hydrology* **475**, 74–83.
- Zhao, W., Du, S. & Emery, J. W. 2017 Object-based convolutional neural network for high-resolution imagery classification. *IEEE Journal of Selected Topics in Applied Earth Observations and Remote Sensing* **10** (7), 3386–3396. <https://doi.org/10.1109/JSTARS.2017.2680324>.
- Zhou, Z., Rahman Siddiquee, M. M., Tajbakhsh, N. & Liang, J. 2018 UNet++: A Nested U-Net Architecture for Medical Image Segmentation. In: Stoyanov, D. *et al.* (eds). *Deep Learning in Medical Image Analysis and Multimodal Learning for Clinical Decision Support*. DLMIA 2018, ML-CDS 2018. Lecture Notes in Computer Science, vol 11045. Springer, Cham, pp. 3–11. [https://doi.org/10.1007/978-3-030-00889-5\\_1](https://doi.org/10.1007/978-3-030-00889-5_1). Accessed 25 Apr 2021.

First received 23 September 2021; accepted in revised form 25 February 2022. Available online 11 March 2022